Electrochemical Model-Based State of Charge and Capacity Estimation for a Composite Electrode Lithium-Ion Battery

Alexander Bartlett, James Marcicki, Simona Onori, Giorgio Rizzoni, Xiao Guang Yang, and Ted Miller

***Abstract*— Increased demand for hybrid and electric vehicles has motivated research to improve onboard state of charge (SOC) and state of health estimation (SOH). In particular, batteries with composite electrodes have become popular for automotive applications due to their ability to balance energy density, power density, and cost by adjusting the amount of each material within the electrode. SOH algorithms that do not use electrochemical-based models may have more difficulty maintaining an accurate battery model as the cell ages under varying degradation modes, such as lithium consumption at the solid-electrolyte interface or active material dissolution. Furthermore, efforts to validate electrochemical model-based state estimation algorithms with experimental aging data are limited, particularly for composite electrode cells. In this paper, we first present a reduced-order electrochemical model for a composite $LiMn_2O_4$-$LiNi_{1/3}Mn_{1/3}Co_{1/3}O_2$ electrode battery that predicts the surface and bulk lithium concentration of each material in the composite electrode, as well as the current split between each material. The model is then used in dual-nonlinear observers to estimate the cell SOC and loss of cyclable lithium over time. Three different observer types are compared: 1) the extended Kalman filter; 2) fixed interval Kalman smoother; and 3) particle filter. Finally, an experimental aging campaign is used to compare the estimated capacities for five different cells with the measured capacities over time.**

***Index Terms*— Battery, estimation, Kalman filter, state of charge (SOC), state of health (SOH).**

NOMENCLATURE

A	Current collector area (m^2).
D_e	Liquid diffusion coefficient (m^2/s).
D_i	Solid diffusion coefficient (m^2/s).
F	Faraday's constant (C/mol).
I	Current (A).
L_c	Total cell thickness (m).
L_i	Electrode thickness (m).
L_{sep}	Separator thickness (m).
N_p	Number of particles in the particle filter.
Q	Process noise covariance.
R	Sensor noise covariance.
$\bar{R}$	Universal gas constant (J/K/mol).
$R_{c,i}$	Ohmic resistance (Ω).
R_i	Particle radius (m).
T	Cell temperature (K).
U_i	Electrode open-circuit voltage (V).
V	Cell voltage (V).
V_e	Liquid-phase voltage across the cell (V).
$\bar{c}_i$	Bulk particle concentration (mol/m^3).
$c_{e,i}$	Electrolyte concentration (mol/m^3).
$c_{\max,i}$	Electrode saturation concentration (mol/m^3).
$c_{s,i}$	Concentration at the particle surface (mol/m^3).
$i_{0,i}$	Exchange current density (A/m^2).
i_e	Liquid-phase current density (A/m^2).
j_i	Solid-phase current density (A/m^2).
k_i	Reaction rate constant ($m^{2.5}/mol^{0.5}/s$).
r	Coordinate along the particle radius, originating at the particle center.
t	Time (s).
t_0^+	Transference number ().
x	Coordinate through-the-thickness of the cell, originating at the anode current collector.
α	Symmetry factor ().
β_i	Current split factor ().
γ	Activity coefficient in electrolyte ().
$\epsilon_{\text{am},i}$	Active material volume fraction ().
ϵ_e	Liquid volume fraction ().
ϵ_i	Active material volume split ().
η_i	Kinetic overpotential (V).
σ_e	Electrolyte conductivity (S/m).
ϕ_e	Electrolyte potential (V).
ϕ_i	Electrode potential (V).
Subscript i	Refers to electrode p, n, LMO, or NMC.

Manuscript received September 15, 2014; revised April 9, 2015; accepted June 12, 2015. Date of publication July 29, 2015; date of current version February 17, 2016. Manuscript received in final form June 14, 2015. This work was supported by Ford Motor Company through the Ford University Research Program. Recommended by Associate Editor S. Varigonda.

A. Bartlett and G. Rizzoni are with the Center for Automotive Research, The Ohio State University, Columbus, OH 43212 USA (e-mail: bartlett.137@osu.edu; rizzoni.1@osu.edu).

J. Marcicki, X. G. Yang, and T. Miller are with the Research and Innovation Center, Ford Motor Company, Dearborn, MI 48124 USA (e-mail: jmarcick@ford.com; xyang11@ford.com; tmille22@ford.com).

S. Onori is with the Automotive Engineering Department, Clemson University, Greenville, SC 29607 USA (e-mail: sonori@clemson.edu).

Color versions of one or more of the figures in this paper are available online at http://ieeexplore.ieee.org.

Digital Object Identifier 10.1109/TCST.2015.2446947

I. INTRODUCTION

VEHICLE electrification continues to be a key topic of interest for automotive manufacturers, with lithium-ion batteries being the technology of choice for hybrid and electric vehicles. State of charge (SOC) and state of health (SOH) estimates are essential inputs to the vehicle's battery management system (BMS) in order for the battery pack to operate

efficiently and safely [1]. Knowledge of SOC allows the BMS to predict the available instantaneous power, while ensuring the battery is operating within safe limits. SOH can be defined in a variety of ways, but typically refers to the degradation of capacity and increase in internal resistance as the battery ages.

Traditionally, SOC and SOH estimates are made with the use of lookup tables or equivalent circuit models (ECMs) consisting of various circuit elements arranged in series or parallel combinations such that the circuit output voltage dynamics mimic that of the battery. Although ECMs are computationally inexpensive, considerable effort must be made to parameterize these models, as the parameters are typically the functions of SOC, temperature, current direction, and battery life [2], [3]. In addition, ECM parameters have little physical meaning, and associated aging models must rely on empirical correlations between SOH and damage factors, such as total current throughput, operating temperature, and depth of discharge [4]. Nonetheless, ECMs have been used successfully for SOC and SOH estimation using extended Kalman filters (EKFs) and other methods [5]–[10].

Recently, increased attention has been given to electrochemical models for SOC and SOH estimation. These models are based on the first principles in porous electrode theory [11] and therefore have the potential to predict cell performance more accurately, as well as provide more information about the internal battery states such as lithium concentrations and reaction overpotentials. However, uncertainty in electrochemical parameters can limit the accuracy of the model and resulting state estimates [22]. Furthermore, electrochemical models rely on partial differential equations (PDEs) to describe lithium diffusion and potential gradients throughout the electrode and electrolyte. Solution methods for PDEs can be computationally expensive, making them illsuited for most practical onboard control and estimation algorithms. A common approximation, known as the single particle model (SPM), is to neglect the spatial variation of concentration and potential throughout the cell and treat each electrode as a single spherical particle, subject to an appropriately scaled, spatially constant current flux. To further facilitate control and estimation, researchers have used various model-order reduction techniques to reduce the PDEs governing diffusion in the spherical particles to low-order ordinary differential equations (ODEs). A reduced-order electrochemical model linearized over a typical operating range was used in [13] in a Kalman filter to estimate the lithium bulk and surface concentration. The authors showed that rather than enforcing strict limits on cell voltage to avoid damaging the battery, enforcing limits on lithium surface concentration and solid/electrolyte potential difference allowed the cell voltage limits to be exceeded without risking electrode saturation/depletion and lithium plating. In [14], an averaged SPM with discretization of the diffusion PDEs was used in a Kalman filter to estimate the bulk and surface concentrations of the positive electrode. The authors recognized weak observability of the complete cell model that includes both electrodes (since the only available measurement depends on the difference between the electrode potentials), and therefore only applied the observer to the positive electrode states.

Loss of spatial information through-the-thickness of the cell is avoided in [2], [16], and [17] using observers capable of handling PDE-based models, although these approaches add to the computational cost. Moura *et al.* [17] also discussed the weak observability of the complete battery system, and approximated the cathode states at their equilibrium, since the average positive concentration can be related to the average negative concentration via conservation of lithium.

There have been a few attempts to use electrochemical-based models for online SOH estimation using dual-SOC/parameter estimation. In [18], the active material fractions of each electrode are estimated along with the bulk and surface SOC, using an unscented Kalman filter. SOH estimation was done in [15], [17], and [19] by applying least squares techniques to estimate the model parameters associated with aging; however, the computational effort required by these approaches may limit their applicability to onboard estimation. In addition, electrochemical model-based SOH estimation algorithms that are validated with experimental aging data are scarce in the literature, and to the best of the authors' knowledge, no such studies have been conducted on cells with composite electrodes. Composite electrodes add to the complexity of the electrochemical model, particularly if it is desired to estimate the SOC and SOH of each electrode material individually.

In this paper, a reduced order electrochemical model is used for SOC/SOH estimation on a composite $LiMn_2O_4$-$LiNi_{1/3}Mn_{1/3}Co_{1/3}O_2$ (LMO-NMC) cathode cell with a graphite anode. The model is based on the SPM with added liquid-phase dynamics, but considers two particles in parallel to represent the composite cathode. This paper then presents a novel numerically inexpensive method for solving for the current split and resulting SOC of each cathode particle (part of preliminary work presented in [20]), and a novel combined SOC/SOH estimation algorithm to estimate capacity fade resulting from loss of cyclable Li. Finally, the estimation algorithm is validated with experimental aging data, by comparing three different observer types (EKF, Kalman smoother, and particle filter).

II. Model Development

The model used in this paper is based on the traditional SPM with the addition of liquid-phase diffusion dynamics to improve model accuracy under high current. Similar models have been presented many times in [2], [13], [14], [16], [18], and [23], however, in order to accommodate the composite LMO-NMC positive electrode, the positive electrode is modeled as two particles acting in parallel (as shown in Fig. 1). Therefore, the potentials of each positive electrode particle model are equal, but the current is split between each particle according to its dynamic effective impedance. This idea of representing a composite electrode as two particles acting in parallel has been presented in [20] and [23].

In the simplest case (at steady state), the measured cell voltage V is just the difference between each electrode open-circuit voltage (OCV) evaluated at their respective steady-state concentrations, i.e., $V = U_p(\bar{c}_p) - U_n(\bar{c}_n)$. However, as the

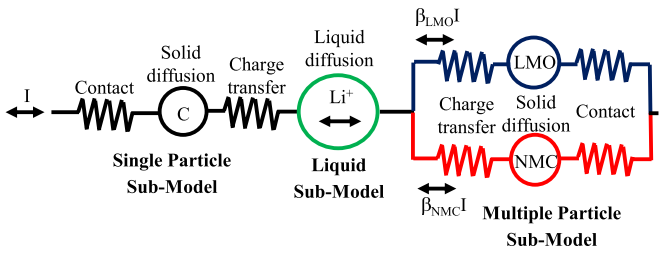

Fig. 1. Schematic of the electrochemical model with a single negative electrode particle and two positive electrode particles acting in parallel.

cell is charged or discharged, various sources of overpotential cause the measured voltage to deviate from this steady-state solution. The overpotentials can be categorized as acting in either the solid (electrode) or liquid (electrolyte) phase, as outlined in Table I, and submodels for each phase can be developed. The dynamic cell voltage (9) is then obtained by subtracting the solid- and liquid-phase overpotentials from the electrode OCVs.

A. Electrode Submodel

The governing equations for Li concentration and electrode potential are shown in (1)–(5) for a given particle i. Subscript i refers to the negative particle, positive LMO particle, or positive NMC particle: n, LMO, or NMC, respectively. Fick's law of mass diffusion in spherical coordinates (4) governs the concentration throughout a spherical particle. The boundary conditions for this PDE are set so as to require symmetry about the particle center and impose a flux at the particle surface, dictated by the current density $j_i(t)$.

The single particle approximation removes the spatial dependence of the current density, allowing it to be defined only as a function of time for a given particle. To form the current density, the applied current is multiplied by a current split factor β_i defined as the fraction of current flowing to a given particle within an electrode. For the single particle negative electrode $\beta_n = 1$, but for the multiple particle positive electrode, β_{LMO} and β_{NMC} vary dynamically and are calculated at each time step, as shown in Section III-A. The current is normalized by the electrode volume, including a parameter ϵ_i representing the active material volume fraction split. Again, for the single particle negative electrode $\epsilon_n = 1$; however, for the multiple particle positive electrode, fitting experimental data gave a material split of $\epsilon_{\text{LMO}} = 0.64$ and $\epsilon_{\text{NMC}} = 0.36$ [23].

The electrode potential (5) is calculated by subtracting the kinetic and ohmic overpotentials from the OCV, evaluated at the particle surface concentration.

B. Electrolyte Submodel

Similar to the solid phase, the liquid phase contains sources of concentration and ohmic overpotential. The concentration of Li throughout the electrolyte is governed by Fick's law in Cartesian coordinates (6), with a source term related to the current density. Since $j_i(t)$ is considered piecewise constant within a given electrode and zero in the separator, (6) is solved separately in each region, subject to coupling boundary conditions that match the concentration and flux at the electrode/separator interfaces.

To obtain the liquid-phase voltage across the entire cell, (7) is integrated directly from $x = 0$ to $x = L_c$, where $i_e(t)$ is considered constant in the separator and linearly decreasing to zero from the electrode/separator boundaries to the current collectors.

III. Model Solution Method

The concentrations of Li in the solid and liquid phases are governed by PDEs; however, this is undesirable if the model is to be used for onboard estimation. Instead, the Padé approximation method for model-order reduction proposed in [22] and [24] was leveraged here to approximate the PDE-based model with a system of low-order ODEs.

A. Solid-Phase Solution

In the solid phase, the important metrics for tracking cell SOC and available power are the particle bulk concentration and particle surface concentration, respectively. A first-order linear transfer function between the bulk concentration and input current is obtained simply by integrating (4) in the Laplace domain from $r = 0$ to $r = R_i$. However, in the case of surface concentrations, a Padé approximation is used to obtain a low-order linear transfer function relating surface concentration to input current for each particle [12], [24]. A third-order approximation is used for the solid-phase PDE, since it gives good accuracy in the frequency range typically seen in a vehicle drive profile [23], while still mitigating the computational effort required for higher order models.

The electrode particle submodel is formulated in state space as follows:

$$\dot{x}_i = A_i x_i + B_i(t)u \tag{10}$$

$$A_i = \begin{bmatrix} 0 & 1 & 0 \\ 0 & 0 & 1 \\ 0 & \dfrac{1}{b_{3,i}} & \dfrac{b_{2,i}}{b_{3,i}} \end{bmatrix}$$

$$B_i(t) = \begin{bmatrix} 0 \\ 0 \\ \mp\left(\dfrac{\beta_i(t)R_i}{3\text{FAL}_i\epsilon_{\text{am},i}\epsilon_i}\right)\dfrac{1}{b_{3,i}} \end{bmatrix}$$

$$\begin{bmatrix} c_{s,i} \\ \bar{c}_i \end{bmatrix} = \begin{bmatrix} a_{0,i} & a_{1,i} & a_{2,i} \\ a_{0,i} & a_{0,i}b_{2,i} & a_{0,i}b_{3,i} \end{bmatrix} x_i$$

$$\phi_i = U_i(c_{s,i}) \pm \eta_i(c_{s,i}, \beta_i(t)u) \pm R_{c,i}\beta_i(t)u \tag{11}$$

where both the bulk and surface concentrations are written as linear combinations of the states x_i, the input u is current, and the output electrode potential is a nonlinear function of the states and input. Note that only the linear combination of the states has any physical meaning, and the states themselves simply represent the dynamics of the third-order Padé approximation. Although there are two separate transfer functions for bulk and surface concentration (first and third orders, respectively), both metrics can be written as linear combinations of the same three states through some algebraic manipulation (as shown in [24]). In other words, there are six total states in the multiple particle positive electrode submodel, and three states in the single particle negative electrode submodel.

TABLE I
GOVERNING EQUATIONS FOR THE SOLID PARTICLE AND LIQUID SUBMODELS

Sub-Model	Variable	Governing Equation	
Solid Particle*	Kinetic overpotential, η_i	$\eta_i(t) = \frac{\bar{R}T}{\alpha F} sinh^{-1}\left(\frac{j_i(t)}{2i_{0,i}(t)}\right)$	(1)
	Exchange current density, $i_{0,i}$	$i_{0,i}(t) = Fk_i\sqrt{c_{s,i}(t)c_{e,i}(t)\left(c_{max,i} - c_{s,i}(t)\right)}$	(2)
	Averaged particle current density, j_i	$j_i(x,t) = j_i(t) = \frac{I(t)\beta_i(t)R_i}{3AL_i\epsilon_{am,i}\epsilon_i}$	(3)
	Li concentration**, c_i	$\frac{\partial c_i}{\partial t} = \frac{D_i}{r^2}\frac{\partial}{\partial r}\left(r^2\frac{\partial c_i}{\partial r}\right), \quad \frac{\partial c_i}{\partial r} = 0 \; at \; r = 0, \quad D_i\frac{\partial c_i}{\partial r} = \mp\frac{j_i(t)}{F} \; at \; r = R_i$	(4)
	Electrode potential**, ϕ_i	$\phi_i(t) = U_i\left(c_{s,i}(t)\right) \pm \eta_i\left(c_{s,i}(t), \beta_i(t)I(t)\right) \pm R_{c,i}\beta_i(t)I(t)$	(5)
Liquid	Li concentration**, c_e	$\epsilon_e\frac{\partial c_e}{\partial t} = D_e\frac{\partial^2 c_e}{\partial x^2} \pm \frac{3(1-t_0^+)}{FR_i}j_i(t)$	(6)
	Electrolyte potential, ϕ_e	$\frac{\partial \phi_e}{\partial x} = \frac{i_e(t)}{\sigma_e} + \frac{2\bar{R}T(1-t_0^+)}{F}(1+\gamma)\frac{\partial \ln(c_e)}{\partial x}$	(7)
	Electrolyte voltage, $V_e = \phi_e(x=0) - \phi_e(x=L_c)$	$V_e(t) = \frac{I(t)(\frac{1}{2}L_p + L_{sep} + \frac{1}{2}L_n)}{\sigma_e A} + \frac{2\bar{R}T(1-t_0^+)}{F}(1+\gamma)\ln\left(\frac{\bar{c}_{e,n}(t)}{\bar{c}_{e,p}(t)}\right)$	(8)
Cell	Cell voltage, V	$V(t) = \phi_p(t) - \phi_n(t) - V_e(t)$	(9)

*Note that subscript, i, refers to the negative particle, positive LMO particle, or positive NMC particle: n, LMO, or NMC, respectively.
**Defining discharge current to be positive, occurrences of $\pm$ or $\mp$ correspond to negative (top sign) and positive (bottom sign) electrodes.

The states are updated in discrete time using a finite difference solution. Constants $a_{0,i}$, $a_{1,i}$, $a_{2,i}$, $b_{2,i}$, and $b_{3,i}$ are obtained from the third- order Padé approximation, and are the functions of the particle radius and diffusion coefficient [12], [24].

Since the positive electrode consists of two particles acting in parallel, the potentials for each particle are equal and the current is multiplied by a current split factor β_i. For the positive electrode, β_i must be solved at each time step to determine how the current is allocated with the constraint that the currents going to each particle sum to the total current (i.e., $\beta_{\text{LMO}} + \beta_{\text{NMC}} = 1$). The β_i term appears nonlinearly in the output equation, so one possible solution method is to guess the value of each β_i, calculate the particle potentials, and iterate until the two particle potentials converge to the same value. This approach could be implemented using a standard nonlinear solver; however, it may not be ideal for online estimation since it requires iteration at each time step. Alternatively, an approximated solution is obtained more quickly using the following linearization procedure.

1) At each time step k, advance the states and concentrations forward in time using the finite difference method

$$x_{i,k} = (Id + \Delta t A_i)x_{i,k-1} + \Delta t B_{i,k-1}u_{k-1}$$
$$\begin{bmatrix} c_{s,i,k} \\ \bar{c}_{i,k} \end{bmatrix} = \begin{bmatrix} a_{0,i} & a_{1,i} & a_{2,i} \\ a_{0,i} & a_{0,i}b_{2,i} & a_{0,i}b_{3,i} \end{bmatrix} x_{i,k} \tag{12}$$

where Id is the identity matrix, Δt is the time step (fixed at 0.1 s), and the current splits in B are from the previous time step.

2) Construct a set of three (non)linear equations, two for the output potentials of each particle and one enforcing that the current splits sum to 1

$$\begin{aligned} f_1 &= \phi_{p,k} = U_{\text{LMO}}(c_{s,\text{LMO},k}) \\ &\quad -\eta_{\text{LMO}}(c_{s,\text{LMO},k}, \beta_{\text{LMO},k}I_k) \\ &\quad -R_{c,\text{LMO}}\beta_{\text{LMO},k}I_k \\ f_2 &= \phi_{p,k} = U_{\text{NMC}}(c_{s,\text{NMC},k}) \\ &\quad -\eta_{\text{NMC}}(c_{s,\text{NMC},k}, \beta_{\text{NMC},k}I_k) \\ &\quad -R_{c,\text{NMC}}\beta_{\text{NMC},k}I_k \\ f_3 &= I_k = \beta_{\text{LMO},k}I_k + \beta_{\text{NMC},k}I_k \end{aligned} \tag{13}$$

where ϕ_p is the total potential of either particle.

3) Remove the nonlinear dependence on β_i in f_1 and f_2 by taking a Taylor series expansion about the current splits at the previous time step

$$\begin{aligned} \phi_{p,k} &\approx f_1|_{\beta_{\text{LMO},k-1}} \\ &\quad + \left.\frac{\partial f_1}{\partial \beta_{\text{LMO}}}\right|_{\beta_{\text{LMO},k-1}} (\beta_{\text{LMO},k} - \beta_{\text{LMO},k-1}) \\ \phi_{p,k} &\approx f_2|_{\beta_{\text{NMC},k-1}} \\ &\quad + \left.\frac{\partial f_2}{\partial \beta_{\text{NMC}}}\right|_{\beta_{\text{NMC},k-1}} (\beta_{\text{NMC},k} - \beta_{\text{NMC},k-1}). \end{aligned} \tag{14}$$

4) Finally, the current splits and potential can be written as the solution to a matrix inversion problem

$$\begin{bmatrix} \left.\frac{\partial f_1}{\partial \beta_{\text{LMO}}}\right|_{\beta_{\text{LMO},k-1}} & 0 & -1 \\ 0 & \left.\frac{\partial f_2}{\partial \beta_{\text{NMC}}}\right|_{\beta_{\text{NMC},k-1}} & -1 \\ I_k & I_k & 0 \end{bmatrix} \begin{bmatrix} \beta_{\text{LMO},k} \\ \beta_{\text{NMC},k} \\ \phi_{p,k} \end{bmatrix}$$
$$= \begin{bmatrix} -f_1|_{\beta_{\text{LMO},k-1}} + \left.\frac{\partial f_1}{\partial \beta_{\text{LMO}}}\right|_{\beta_{\text{LMO},k-1}} \beta_{\text{LMO},k-1} \\ -f_2|_{\beta_{\text{NMC},k-1}} + \left.\frac{\partial f_2}{\partial \beta_{\text{NMC}}}\right|_{\beta_{\text{NMC},k-1}} \beta_{\text{NMC},k-1} \\ I_k \end{bmatrix}. \tag{15}$$

In addition to the current splits, solving (15) also gives a value for the linearized output electrode potential $\phi_{p,k}$; however, this value is discarded at this point. Instead, the original nonlinear output (11) is used to calculate the electrode potential, thereby avoiding the voltage prediction inaccuracies seen with the linearization process. In this way, the errors associated with the output linearization only affect the calculation of β_i, and not the calculation of the output voltage (apart from the indirect effect from β_i).

Fig. 2 shows the predicted current split and resulting SOC for each cathode material for a constant 1C discharge. The predicted voltage shows good agreement with the measured voltage (more rigorous validation of the model was done in [23]). More LMO is utilized initially at high voltages, until it is nearly depleted, at which point

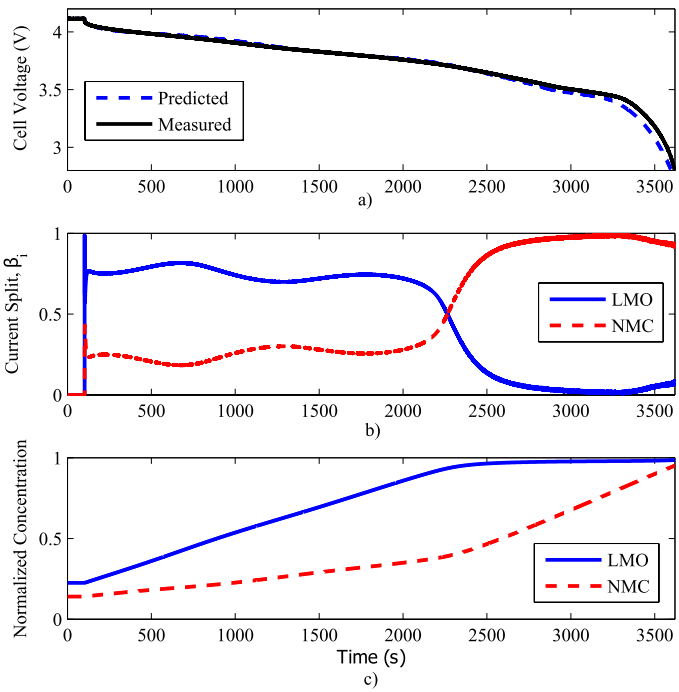

Fig. 2. (a) Model prediction of the cell voltage compared with the measured voltage. (b) Current split factor β_i for each material. (c) Normalized concentration for each material for a 1C constant current discharge.

NMC carries the bulk of the current for the remainder of the discharge. This result is consistent with an *in situ* X-ray diffraction (XRD) study of a composite LMO-NMC cathode [25].

One drawback of this electrode model with parallel particles is that, for instances, when the current abruptly changes in magnitude and/or direction, the calculated β_i for a given particle can greatly exceed 1 (resulting in a large negative β_i for the other particle). While it is unclear if this occurrence makes physical sense, it typically lasts for only a few time steps before the β_is return to more sensible values between 0 and 1. Furthermore, these are usually instances when the total current is near zero, so a large β_i does not translate into a large current going to a given particle.

It should also be noted that if the state estimate has not yet converged, there will be some error in the calculation of β_i, since it relies on the current state estimate. This would in turn cause an error in the state estimate calculated at the next time step. However, this does not affect the stability of the state estimate. Even if there is an extreme error in β_i, eventually the concentration estimate of one of the materials will become saturated, which will decrease β_i for that material, thereby driving the estimate back toward the correct value. Instead, calculation of β_i using an unconverged state estimate can be categorized as a model error, which may affect the estimate accuracy, but will not cause the estimate to become unstable. Furthermore, in a real automotive application, there are periodic instances when the current is near zero, and the influence of β_i is negligible. During these times, the state estimate can converge accurately, thereby minimizing the error in β_i once the current resumes.

To summarize the solution method for the composite positive electrode: at each time step k, the states are updated in discrete time using the calculated values for $\beta_{i,k-1}$ at the previous time step (10), the values for $\beta_{i,k}$ at the current time step are then calculated using the linearization method outlined above (15), and finally the output potentials are calculated using the updated states and precalculated values for $\beta_{i,k}$ (11).

B. Liquid-Phase Solution

Equation (8) governs the liquid-phase voltage across the cell and depends on the Li-ion concentrations in the liquid at each electrode. Therefore, the PDE governing Li concentration is solved at each electrode end ($x = 0$ and $x = L_c$) using a first-order Padé approximation. This results in two first-order transfer functions relating liquid-phase concentration at each electrode to the current input. Only a first-order approximation is needed for the liquid phase concentration, since it shows a very good accuracy throughout the frequency range of interest [22]. In state space, the two states in x_e represent the liquid concentrations at each electrode, the input u is current, and the output voltage is a nonlinear function of the states and input

$$\dot{x}_e = A_e x_e + B_e u \tag{16}$$

$$A_e = \begin{bmatrix} \dfrac{1}{b_{1,e,p}} & 0 \\ 0 & \dfrac{1}{b_{1,e,n}} \end{bmatrix}$$

$$B_e = \left(\frac{1-t_0^+}{\mathrm{FAL}_c\epsilon_e}\right)\begin{bmatrix} -\dfrac{1}{b_{2,e,p}} \\ \dfrac{1}{b_{2,e,n}} \end{bmatrix}$$

$$\begin{bmatrix} \bar{c}_{e,p} \\ \bar{c}_{e,n} \end{bmatrix} = \begin{bmatrix} 1 & 1 \end{bmatrix} x_e$$

$$V_e = \frac{u\left(\frac{1}{2}L_p + L_{\mathrm{sep}} + \frac{1}{2}L_n\right)}{\sigma_e A} + \frac{2\bar{R}T\left(1-t_0^+\right)}{F}(1+\gamma)\ln\left(\frac{\bar{c}_{e,n}}{\bar{c}_{e,p}}\right). \tag{17}$$

Again, the constants $b_{1,e,p}$, $b_{1,e,n}$, $b_{2,e,p}$, and $b_{2,e,n}$ are obtained from the first-order Padé approximation [12].

IV. System Observability

In order to design an observer, the system must be shown to be observable (or at least detectable) to ensure that the state estimates converge to the true states in a finite time [26]. Observability of a system requires that the state trajectory can be uniquely reconstructed based solely on the knowledge of the output measurements and inputs. Local observability of a nonlinear system can be shown with the use of Lie derivatives [26]. The Lie derivatives L_f for a nonlinear system with state dynamics $\dot{x} = f(x,u)$ and output equation $y = g(x,u)$ form the vector

$$l(x,u) = \begin{bmatrix} y \\ \dot{y} \\ \vdots \\ y^{(n-1)} \end{bmatrix} = \begin{bmatrix} g \\ \dot{g} \\ \vdots \\ g^{(n-1)} \end{bmatrix} = \begin{bmatrix} L_f^0 \\ L_f^1 \\ \vdots \\ L_f^{n-1} \end{bmatrix}. \tag{18}$$

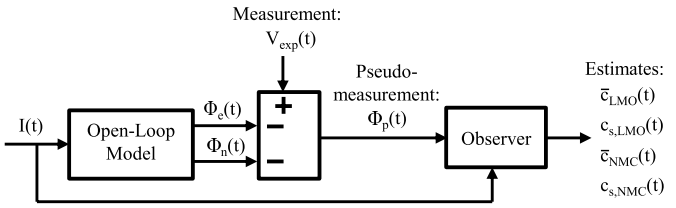

Fig. 3. Block diagram of the algorithm for estimating the positive electrode states. The negative electrode and liquid phase are simulated open loop in order to generate a pseudomeasurement of the positive electrode potential. Alternatively, the negative electrode states could be estimated by simulating the positive electrode open loop.

The observability matrix is obtained by taking the Jacobian of the Lie derivative vector

$$\mathcal{O} = \begin{bmatrix} \dfrac{\partial L_f^0}{\partial x_1} & \cdots & \dfrac{\partial L_f^0}{\partial x_n} \\ \vdots & & \vdots \\ \dfrac{\partial L_f^{n-1}}{\partial x_1} & \cdots & \dfrac{\partial L_f^{n-1}}{\partial x_n} \end{bmatrix}. \tag{19}$$

An observability matrix with full rank implies that the states are locally observable. However, performing this exercise on the complete battery model, including both positive and negative electrodes, results in an observability matrix with full rank but with a high (two-norm) condition number ($\approx 10^{10}$) for typical parameter and input values. This is an intuitive result, as it should be difficult to uniquely identify the states of both electrodes if the only available measurement is the difference between positive and negative electrode potentials.

To help facilitate observer design, the degree of observability can be improved using one of the two methods. In the first method, the states of only one electrode are estimated at a given time, while the liquid phase and opposite electrode states are simulated open loop. For example, if the positive electrode states are to be estimated, the negative electrode and liquid-phase potentials are calculated using the open-loop model. These potentials are subtracted from the measured cell voltage to obtain a pseudomeasurement of positive electrode potential. This pseudomeasurement is then used as feedback in the observer to estimate the positive electrode states. The process is outlined in Fig. 3 for estimating the positive electrode states. However, clearly, since the liquid phase and one electrode are simulated open loop, any initial condition and model errors in these submodels will be projected forward to adversely affect the opposite electrode estimate.

An alternative to relying on an open-loop simulation of one electrode is to use a steady-state approach, where the bulk concentration of one electrode is related to the bulk concentration of the other, via conservation of lithium

$$\frac{\frac{\bar{c}_p}{c_{\max,p}} - y_f}{y_0 - y_f} = \frac{\frac{\bar{c}_n}{c_{\max,n}} - x_f}{x_0 - x_f} \tag{20}$$

where y_0 to y_f is the normalized concentration operating range of the positive electrode and x_0 to x_f is the operating range of the negative electrode, as shown in Fig. 6. Note that x_0 and y_0 are the normalized concentrations at the upper voltage limit, while x_f and y_f correspond to the lower voltage limit. This steady-state approach was applied in [14] and [17] to estimate the cell SOC. The advantage of this method is that it enforces conservation of lithium in the cell, which is a good approximation over a given drive cycle. However, this approach neglects the diffusion dynamics of one electrode, which may have implications in estimation of available power. In addition, like the open-loop method, it relies on accurate initialization of the normalized concentration operating range of each electrode, so any errors in the x_0, x_f, y_0, and y_f parameters will adversely affect the state estimates.

Both the open-loop and steady-state approaches essentially limit the estimated states to one electrode, and by doing so, the condition number of the observability matrix is reduced by several orders of magnitude (down to $\approx 10^6$). In this paper, results using the open-loop approach are shown, although testing of both methods revealed only slight differences in the SOC and capacity estimation results.

Even though the estimated states are limited to just one electrode whose electrode submodel must be shown to be observable with respect to a pseudomeasurement of its output potential. The electrode submodel has linear state dynamics (10) with a nonlinear output (11). The goal is to show that all three states in the submodel are observable, allowing for the estimation of both the surface and bulk electrode concentrations $c_{s,i}$ and $\bar{c}_i$. The OCV term U_i is often calculated via lookup table or by an empirical functional fit; however, to make calculating the Lie derivatives easier computationally, a cubic spline is used to evaluate the OCV at a given concentration. The cubic spline is continuously differentiable at the spline transitions up to the second derivative, so proving the observability for a given spline segment guarantees observability for the entire OCV curve. Substituting an arbitrary cubic spline segment for the OCV term, the electrode submodel becomes

$$\dot{x}_i = f(x_i, u) = A_i x_i + B_i(t) u \tag{21}$$

$$\begin{aligned} y &= g(x_i, u) \\ &= \left(\frac{s_{3,i} c_{s,i}^3}{c_{\max,i}^3} + \frac{s_{2,i} c_{s,i}^2}{c_{\max,i}^2} + \frac{s_{1,i} c_{s,i}}{c_{\max,i}} + s_{0,i} \right) \\ &\quad - \eta_i(c_{s,i}, \beta_i u) - R_{c,i} \beta_i u \end{aligned} \tag{22}$$

where $s_{0,i}$, $s_{1,i}$, $s_{2,i}$, and $s_{3,i}$ are the OCV cubic spline coefficients, and $c_{s,i}$ is a linear function of the states, as shown in (10).

The resulting Lie derivatives and observability matrix are too lengthy to show here, in particular due to differentiating the hyperbolic sine function in η_i, but the process is outlined in the Appendix. The observability matrix has full rank for nonzero parameter values, proving that the electrode particle submodel is locally observable with respect to a psuedomeasurement of its potential. Although the both positive and negative electrodes are observable, the negative electrode states are more sensitive to model or sensor errors. This is due to the flat shape of the negative electrode OCV in certain concentration ranges, where a small error in voltage can produce a large error in estimated concentration. The implications of the flat negative OCV will be discussed in Section VII-B.

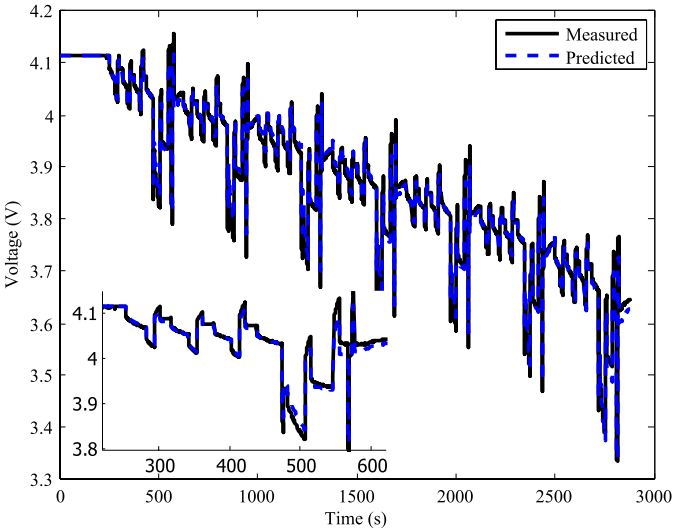

Fig. 4. Model prediction of the cell voltage compared with the measured voltage for the CD current profile used in the aging campaign, as shown in Fig. 10(a).

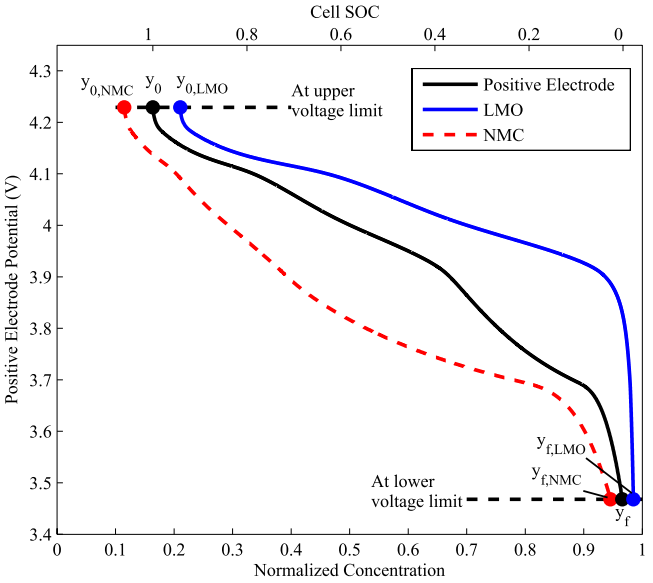

Fig. 5. Initial and final concentrations are defined at the upper and lower cell voltage limits. The overall initial and final normalized concentrations y_0 and y_f correspond to a cell SOC (top axis) of 1 and 0, respectively.

V. Experimental Data Collection

An aging campaign was conducted using 15-Ah (nominal) automotive pouch cells with a composite LMO-NMC cathode and graphite anode cycled under different operating conditions. The cells were cycled using the charge depleting (CD) current profile defined by the United States Advanced Battery Consortium [27], which is representative of a plug-in hybrid vehicle (PHEV) application. The CD current profile is shown in Fig. 10, and was repeated until the cell reached 45%, 35%, or 25% SOC. Each CD cycle was followed by a constant current constant voltage (CCCV) charge at a C/3, 3C/2, or 5C charge rate. All cells were maintained at a constant of 30 °C by Peltier junctions. Periodic capacity assessments were conducted at approximately every 2000–5000 Ah of throughput. The capacity assessments involved an initial 1C CCCV charge to 4.15 V, followed by a 1C discharge to 2.8 V, followed by a second 1C CCCV charge. The measured capacity was taken as the average of the discharge and charge capacities. The electrode OCVs (as shown in Figs. 5 and 8) and the parameter values from [23] were used to calibrate the model.

An example of the open-loop model fit for the dynamic CD profile used in the experimental aging campaign is shown in Fig. 4. The root-mean-squared error over this test is 14 mV with a maximum error of 75 mV.

It should be noted that no significant resistance rise was observed in the cells used in this paper, allowing the impedance-related model parameters to be treated as constant. The change in 1-s resistance was generally less than 0.1 mΩ over the course of the aging campaign. However, for different aging conditions or electrode chemistries, resistance rise can be significant and online estimation of these parameters may be required to maintain model accuracy.

VI. Observer Design

Three different observer types are used for state estimation in order to compare their estimation accuracy and computational effort. Specifically, the EKF, fixed interval Kalman smoother, and particle filter are implemented and compared. The implementation of each observer can be found in the literature, but brief descriptions will be given here.

The EKF [5], [6], [30] is an extension of the Kalman filter, optimal for linear systems, to nonlinear systems where the process and sensor noise are assumed to be uncorrelated, white, and Gaussian. As is typical of model-based observers, the EKF involves both a prediction step and a correction step. In the prediction step, open-loop predictions of the state vector and output are obtained from the model. The state prediction is then adjusted in the correction step by utilizing feedback from the measurement. The feedback gain (optimal for a linear system) is calculated at each time step, based on the knowledge of the model and noise covariance matrices. For nonlinear systems, calculation of the observer gain relies on a linearization of the nonlinear system dynamics and output equation. In practice, the process and sensor noise covariance matrices are not necessarily known, and there may be significant model errors. Therefore, the noise covariances are typically used as tuning factors to achieve the desired observer behavior for a particular system.

The fixed interval Kalman smoother (or forward–backward smoother) has the potential to improve upon the traditional EKF by essentially running the filter twice, once forward in time and once backward in time, over a fixed interval of measurements [30], [35]. Once both forward and backward estimates are obtained, they are combined in an optimal way to minimize the estimation error covariance. The resulting smoothed estimate has a smaller estimate error covariance than either of the forward or backward estimates individually. The obvious disadvantage of this method, other than the added computational effort, is that the estimation can no longer be performed in real time. It is necessary to wait until all the measurements within the interval become available before

TABLE II
TUNING PARAMETERS FOR EACH OBSERVER TYPE

Positive electrode state estimation (Obs_p)

Observer	Parameter
EKF*	$Q = 10^{-19}\begin{bmatrix} 1500 & 0 & 0 \\ 0 & 1.5 & 0 \\ 0 & 0 & 0.0015 \end{bmatrix}$
	$R = 2.24 \times 10^{-4}$

Negative electrode state estimation (Obs_n)

Observer	Parameter
EKF	$Q = 10^{-17}\begin{bmatrix} 2500 & 0 & 0 \\ 0 & 2.5 & 0 \\ 0 & 0 & 0.0025 \end{bmatrix}$
	$R = 2.45 \times 10^{-5}$
Kalman Smoother	$Q = 10^{-17}\begin{bmatrix} 2500 & 0 & 0 \\ 0 & 2.5 & 0 \\ 0 & 0 & 0.0025 \end{bmatrix}$
	$R = 2.45 \times 10^{-5}$
Particle Filter**	$Q = 10^{-15}\begin{bmatrix} 1200 & 0 & 0 \\ 0 & 1.2 & 0 \\ 0 & 0 & 0.0012 \end{bmatrix}$
	$R = 2.45 \times 10^{-5}$
	$N_p = 10$

*Σ_w and Σ_v are identical for LMO and NMC particles.
**Gaussian sensor and process noise are assumed.

even the initial smoothed state estimate can be obtained. However, for SOH estimation this is not a significant problem, since in practice aging parameters change very slowly and need not be continuously updated in real time.

The particle filter is a Monte Carlo method used for state estimation by representing the posterior probability density function (pdf), i.e., the conditional pdf of the state given a measurement, by a set of weighted random samples or particles [30]–[32]. Each particle is assigned a weight based on the likelihood that it represents the true state. The advantage of the particle filter is that it does not require linearization of the nonlinear model, nor does it require that the process and sensor noise be Gaussian. Choosing the number of particles to sample N_p represents a tradeoff between estimate accuracy and computational effort.

The relevant parameters for each observer are outlined in Table II, and were tuned to achieve a desired compromise between model error robustness, state convergence time, and computational effort.

VII. METHODS FOR SOC/SOH ESTIMATION

A. Estimating Cell SOC

Estimating the states of one of the electrode particle submodels gives an estimate of both bulk and surface concentrations of the particle; however, without the use of *in situ* XRD or similar techniques, it is only possible to experimentally validate the bulk concentration estimate by comparing it against Coulomb counting, or integrating the measured current over time

$$\mathrm{SOC}_{\mathrm{exp}} = \mathrm{SOC}_0 - \frac{1}{3600C}\int_{t_0}^{t_f} I(t)dt. \tag{23}$$

The initial SOC_0 is taken from a cell level OCV–SOC lookup table and the cell capacity C is obtained from the experimental capacity in ampere-hours measured between the two voltage limits. In this paper, the positive electrode state estimates are validated with Coulomb counting because the positive electrode is typically the power limiting electrode. In addition, the positive electrode OCV is steeper than the negative in most concentration ranges, so the positive state estimates are generally less sensitive to voltage errors. Since the observer estimates the electrode concentrations of each composite material (ranging from 0 to the saturation concentration of the electrode material), some effort must be made to convert the concentration estimates to a cell level SOC (ranging from 0 to 1, defined at the cell voltage limits) in order to compare the result with Coulomb counting. The positive electrode bulk concentration estimates for each of the composite materials are first converted to an overall positive electrode bulk SOC estimate via conservation of lithium within the electrode

$$\hat{\mathrm{SOC}}_p = \frac{\bar{c}_{\mathrm{LMO}}\epsilon_{\mathrm{LMO}} + \bar{c}_{\mathrm{NMC}}\epsilon_{\mathrm{NMC}}}{c_{\mathrm{max,LMO}}\epsilon_{\mathrm{LMO}} + c_{\mathrm{max,NMC}}\epsilon_{\mathrm{NMC}}}. \tag{24}$$

This overall positive electrode bulk SOC operates between an initial and final value y_0 and y_f corresponding to the upper and lower voltage limits. The initial and final values y_0 and y_f are the functions of the initial and final values of each composite material

$$y_0 = \frac{y_{0,\mathrm{LMO}}c_{\mathrm{max,LMO}}\epsilon_{\mathrm{LMO}} + y_{0,\mathrm{NMC}}c_{\mathrm{max,NMC}}\epsilon_{\mathrm{NMC}}}{c_{\mathrm{max,LMO}}\epsilon_{\mathrm{LMO}} + c_{\mathrm{max,NMC}}\epsilon_{\mathrm{NMC}}} \tag{25}$$

$$y_f = \frac{y_{f,\mathrm{LMO}}c_{\mathrm{max,LMO}}\epsilon_{\mathrm{LMO}} + y_{f,\mathrm{NMC}}c_{\mathrm{max,NMC}}\epsilon_{\mathrm{NMC}}}{c_{\mathrm{max,LMO}}\epsilon_{\mathrm{LMO}} + c_{\mathrm{max,NMC}}\epsilon_{\mathrm{NMC}}}. \tag{26}$$

Finally, the estimated cell level $\hat{\mathrm{SOC}}$ is calculated by

$$\hat{\mathrm{SOC}} = 1 - \frac{\hat{\mathrm{SOC}}_p - y_0}{y_f - y_0}. \tag{27}$$

An example of this procedure is shown in Fig. 5 for a constant current discharge. Once a cell level SOC estimate is calculated, it can be validated against the experimental SOC from Coulomb counting.

B. Estimating Capacity

Unlike with SOC estimation, capacity estimates do not necessarily need to be made in real time, since capacity only changes significantly over months or years of usage. This gives some flexibility in making capacity estimates, and it is possible to wait for ideal conditions before making an estimate.

For the composite LMO-NMC cells tested, previous work used differential capacity analysis to show the dominant aging mechanism to be solid-electrolyte interface (SEI) layer growth at the negative electrode [23]. Although other mechanisms, such as loss of active material, may become significant during later stages of life [33], [34] or at high temperatures, only loss of cyclable lithium is considered in this paper. The SEI layer grows as a result of a lithium-consuming side reaction between the electrolyte solvent and the electrode material. This causes a shift in the normalized concentration operating ranges of the positive (y_0 to y_f) and negative (x_0 to x_f) electrodes, shown in Fig. 6, as the electrodes becomes less lithiated overall.

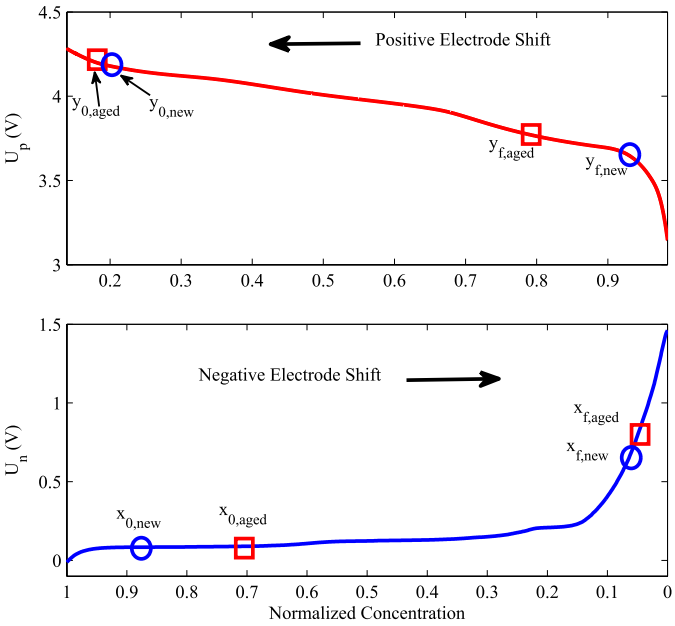

Fig. 6. Example of a shift in the electrode operating range from a new to an aged cell, as cyclable lithium is lost to SEI growth. In each electrode, the operating range tends to shift to a less lithiated state.

Again, x_0 and y_0 correspond to the upper voltage limit, while x_f and y_f correspond to the lower voltage limit.

The normalized concentration operating range of either electrode can be converted to a capacity in ampere-hours by

$$\begin{aligned} C &= (x_0 - x_f)c_{\max,n}\mathrm{FAL}_n\epsilon_{\mathrm{am},n}\epsilon_n/3600 \\ &= \frac{\mathrm{FAL}_p\epsilon_{\mathrm{am},p}}{3600}((y_{f,\mathrm{LMO}} - y_{0,\mathrm{LMO}})c_{\max,\mathrm{LMO}}\epsilon_{\mathrm{LMO}} \\ &\qquad + (y_{f,\mathrm{NMC}} - y_{0,\mathrm{NMC}})c_{\max,\mathrm{NMC}}\epsilon_{\mathrm{NMC}}). \quad (28) \end{aligned}$$

This is the realizable capacity between the two cell voltage limits and so is identical for each electrode. Therefore, an estimate of the normalized concentration range of a given electrode can be used to obtain an estimate of cell capacity. First, it should be noted that a direct estimate of the lower concentration limit x_f or y_f cannot be relied upon, since a complete discharge of the battery is not expected in practice. The upper concentration limit x_0 or y_0, however, can be expected to be reached during regular charging. Again, since estimation is only performed on one electrode at a time, determining which electrode normalized concentration range to estimate presents an interesting dilemma. The positive electrode states are less sensitive to voltage errors due to the steep positive OCV curve, but the shift in y_0 for a given δC is very small and difficult to detect. Conversely, the negative electrode states are more sensitive to voltage errors due to a flatter OCV curve, but the shift in x_0 is large and easier to detect. Through experimentation, it was determined that the latter approach gave the best results, as the problems due to the flat OCV can be mitigated with careful selection of when to make an estimate. Therefore, the loss in capacity is determined by estimating the shift in x_0. Since the concentration corresponding to x_f is not encountered in practice x_f is related to x_0 by a lookup table, via offline

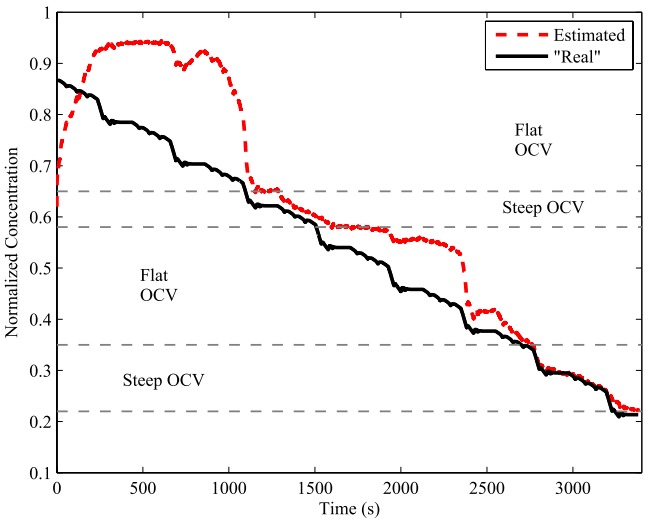

Fig. 7. Demonstration of the increased negative electrode estimation error in regions where the OCV is flat. A perfect model is assumed in order to generate pseudodata. A constant 10-mV voltage measurement bias is applied to the pseudodata voltage. The pseudodata are then used as the measurement in the EKF to estimate the negative electrode states.

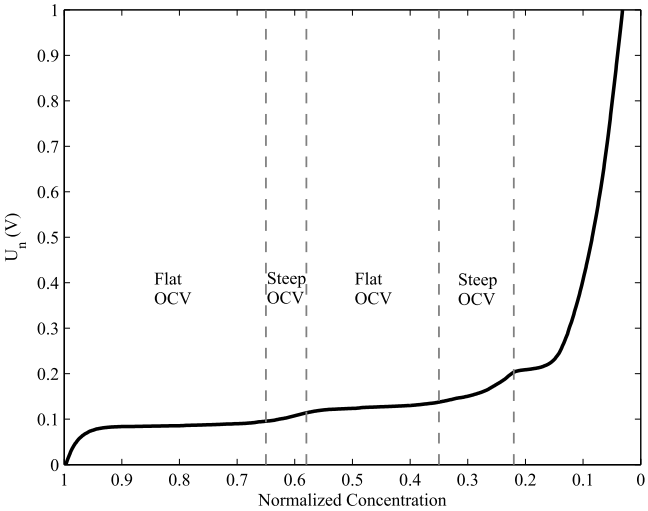

Fig. 8. Negative electrode OCV (measured from half cell experiment), showing regions where the OCV is flat or steep.

simulation of the model during a low rate constant current discharge. For various values of x_0 corresponding to the upper voltage limit, the model is simulated to determine the x_f corresponding to the lower voltage limit.

1) Estimating Capacity From an Estimate of x_0: Estimating x_0 and x_f is not as straightforward as simply estimating the electrode concentration at a given point in time. The negative electrode OCV has regions that are relatively flat, which implies sensitivity to voltage model or sensor error. This can be demonstrated by estimating the negative electrode states for a CD cycle, where a perfect model is assumed but a 10-mV voltage measurement bias is introduced (Fig. 7). The negative electrode normalized concentration estimate is poor in regions where the OCV is flat (Fig. 8), but converges toward the true value in regions where the OCV is steeper. The steep OCV regions are around normalized concentrations of 0.58–0.65 and 0.22–0.35, with the latter region being

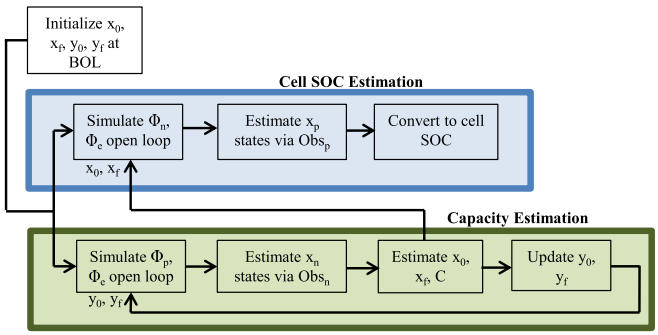

Fig. 9. Block diagram of the combined cell SOC/SOH estimation algorithm.

the steeper of the two. However, the goal is to estimate x_0 (essentially, the negative electrode initial condition, if the cell begins at a fully charged state), which is typically greater than 0.65, and may lie in a flat region of the OCV. This can be observed in Fig. 7, as the estimate is unable to accurately converge from an initial condition error at the beginning of the discharge. Therefore, to obtain an estimate of x_0, the strategy is to wait until the estimate is likely converged (i.e., wait until a steep OCV region is reached), and then calculate the initial state by Coulomb counting backward in time starting from the converged state.

Further complicating the problem, any estimation of the negative electrode requires simulating the positive electrode model open loop. This requires knowledge of the positive electrode range y_0 and y_f, which also change as the cell ages. However, y_0 and y_f at a given stage of life are directly related to x_0 and x_f according to the following procedures:

1) estimate x_0 and x_f;
2) calculate $U_{0,n}$ and $U_{f,n}$ at the initial and final state via negative OCV lookup;
3) calculate $U_{0,p} = 4.15 + U_{0,n}$ and $U_{f,p} = 2.8 + U_{f,n}$, since the upper and lower cell voltage limits remain at 4.15 and 2.8 V throughout the battery life;
4) calculate $y_{0,\mathrm{LMO}}$, $y_{f,\mathrm{LMO}}$, $y_{0,\mathrm{NMC}}$, and $y_{f,\mathrm{NMC}}$ via the corresponding positive OCV lookup;
5) calculate y_0 and y_f using (25) and (26).

The complete SOC/SOH estimation procedure is outlined in Fig. 9. The observer is applied to the positive states to continuously estimate the cell SOC. Then after every CD cycle, an estimate of x_0 and x_f is obtained by waiting until either the mid-SOC region or low-SOC region is reached. Finally, capacity is calculated from estimates of x_0 and x_f.

Essentially, there are dual observers running in parallel, one that estimates the positive electrode states to obtain cell SOC Obs_p (simulating the negative electrode and liquid-phase open loop) and one that estimates the negative electrode states to obtain capacity Obs_n (simulating the positive electrode and liquid-phase open loop). Clearly, the submodels that are simulated open loop will not be able to correct for initial condition errors. It is therefore the role of the capacity estimation algorithm to correctly update the x_0 and y_0 initial conditions so that the open-loop submodels remain accurate.

The propagation of error in the combined SOC/SOH estimation algorithm is a particularly important topic to study. For example, in the SOH estimation block in Fig. 9, the estimated parameter y_0 is fed into the next open-loop prediction of the positive electrode. It is conceivable that a small error in a given y_0 estimate could contribute to additional error in the next y_0 estimate, and so forth, resulting in a positive feedback that would greatly amplify the initial error. An initial investigation into this problem has shown the x_0/y_0 estimates to be robust enough that this positive feedback is avoided; however, this topic will be studied further in future work. Particularly, the error in the SOC/SOH estimates should be quantified, or at least bounded. One advantage in the algorithm design is that the only exchange of information between the two observers comes from the update of x_0 and x_f that are fed into the open-loop simulation of the negative electrode used by Obs_p. Since the parameters x_0 and x_f change only very slowly over hundreds of ampere-hours, they have a negligible effect on the stability of the cell SOC estimation, which operates over a much faster time scale.

C. Initializing the Electrodes

Estimates of the electrode composition ranges, x_0, x_f, y_0, and y_f, are used to initialize the electrode concentrations at the beginning of a given cycle. Assuming that the cell is at equilibrium at the start of the cycle, the initial SOC of each electrode is identical, when normalized by its composition range

$$\frac{\hat{\mathrm{SOC}}_{p,0} - y_f}{y_0 - y_f} = \frac{\hat{\mathrm{SOC}}_{n,0} - x_f}{x_0 - x_f} \tag{29}$$

where $\hat{\mathrm{SOC}}_p$ is defined in (24) for the composite electrode and $\hat{\mathrm{SOC}}_n$ is simply equal to $\bar{c}_n / c_{\max,n}$. In addition, the initial cell voltage must equal the difference between the positive and negative OCV, evaluated at their respective concentrations. In the case of the composite positive electrode, both the LMO or NMC OCVs may be used (forming two separate equations). Finally, a nonlinear iterative solver is used to solve for the initial SOC of each electrode active material (three equations and three unknowns).

VIII. Results

To validate the combined SOC/SOH estimation algorithm, the estimation was performed on five different automotive pouch cells aged under different conditions. The five cells differ in the final SOC that was reached in CD mode and in the charge rate.

A. SOC Estimate Validation

The cell SOC estimate is compared with SOC from Coulomb counting in Fig. 10 for Cell 2 under a CD PHEV cycle taken at the beginning of life (BOL). Only the results using the EKF are shown, since it requires the least computational effort of the three observer types considered and is therefore the most practical for real-time SOC estimation. The cell SOC estimate converges quickly from an imposed initial condition error, and shows good agreement with the SOC from Coulomb counting, with a maximum error of less than 2% during the CD portion of the cycle. Increased estimate

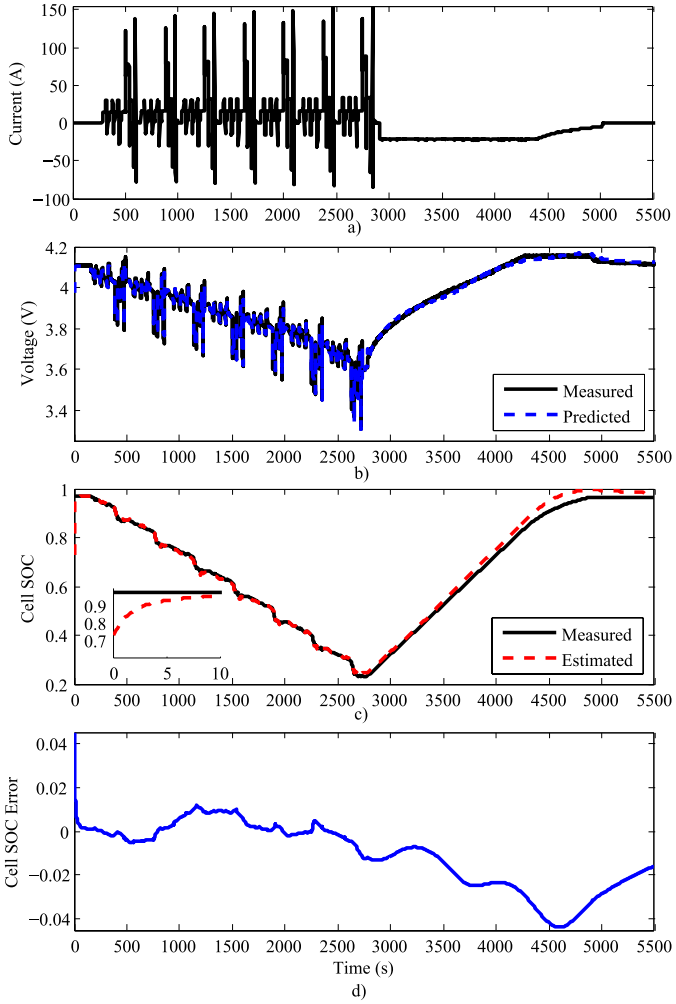

Fig. 10. Estimation results for Cell 2 over a CD CCCV charge profile. (a) Imposed current profile. (b) Predicted and measured cell voltage. (c) Cell SOC estimate and SOC from Coulomb counting, showing convergence from an initial condition error. (d) Cell SOC estimate error.

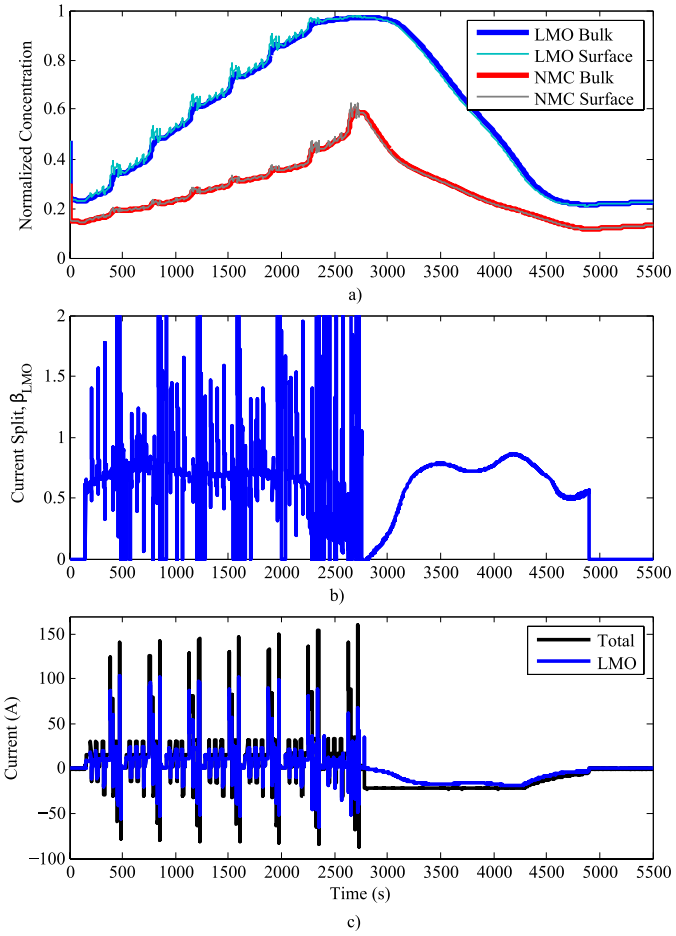

Fig. 11. Estimation results for Cell 2 over a CD CCCV charge profile. (a) Estimated bulk and surface normalized concentrations for each composite material. (b) Current split factor β_{LMO} (β_{NMC} is simply equal to 1—β_{LMO}). (c) Current (in amperes) going to the LMO particle compared with the total current.

error up to 4% is seen during the constant voltage charge due to poor open-loop model agreement during this portion of the charge. This level of SOC estimate error is similar among all the cells tested.

Fig. 11 shows the estimated surface and bulk concentrations of each individual composite electrode material over the same PHEV cycle, as well as the current split factor; although again, these cannot be easily validated experimentally. Note that, despite the fact that the current split factor exceeds 1 in some instances, this does not translate into a large current going to the particle, as these are instances when the total current is small. In other words, there are no large current spikes going to a particle that could cause a large error in the state trajectory, as indicated by Fig. 11(c).

B. Capacity Estimate Validation

For capacity estimation, the x_0 estimate is obtained by waiting for state convergence in a steep OCV region before Coulomb counting backward to the beginning of the discharge. Therefore, a single capacity estimate is obtained after each CD cycle is complete. As noted previously, the low-SOC region from 0.22 to 0.35 is the preferred region to record the converged state since it corresponds to a steeper OCV than the mid-SOC region between 0.58 and 0.65; however, some cells are not sufficiently discharged to reach the low-SOC region. In these cases, the converged state estimate is taken in the mid-SOC region (specifically at 0.6). Otherwise, if the cell does reach the low-SOC region, the estimate at mid-SOC is discarded and the converged state estimate is taken at the midway point between 0.35 and the lowest concentration reached (assuming the value is not less than 0.22). Capacity estimates for the five cells are shown in Figs. 12–16, and are compared with the measured capacities at periodic assessments. For each capacity estimate, it is noted whether the estimate relied on a converged state estimate taken in the low-SOC region or mid-SOC region. In addition, for each cell, three different estimation methods (EKF, Kalman smoother, and particle filter) are compared. The estimation results are summarized in Table III.

The first thing to note is that after each capacity assessment, the estimates show some small amount of capacity recovery. This is expected since the cells would typically rest for

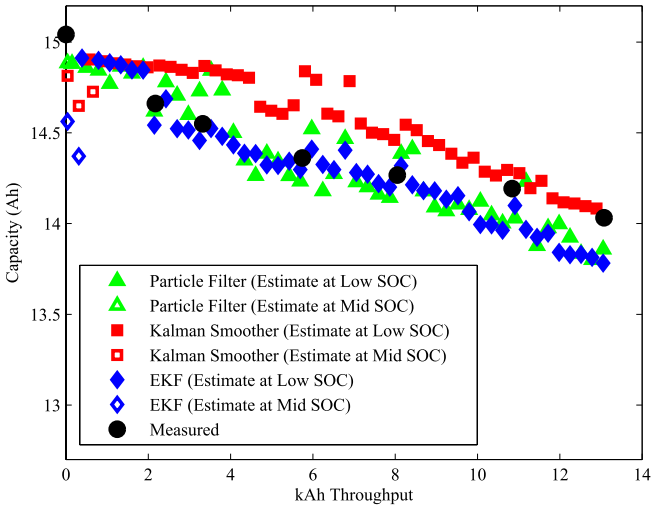

Fig. 12. Capacity estimation results for Cell 1 aged with a CD profile to 25% SOC charged at C/3.

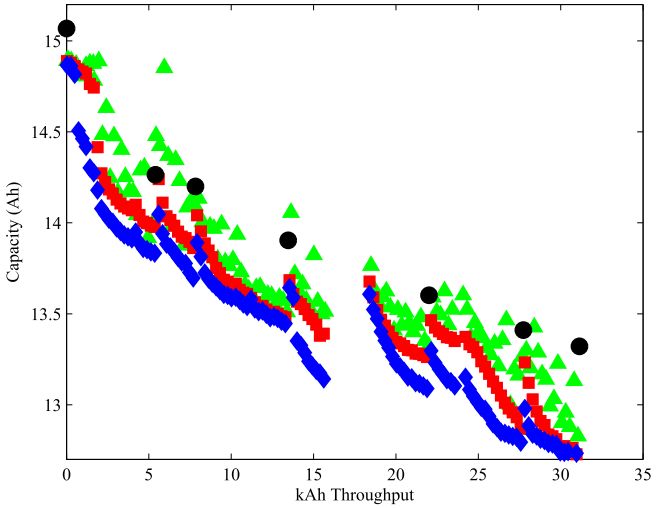

Fig. 14. Capacity estimation results for Cell 3 aged with a CD profile to 25% SOC charged at 5C.

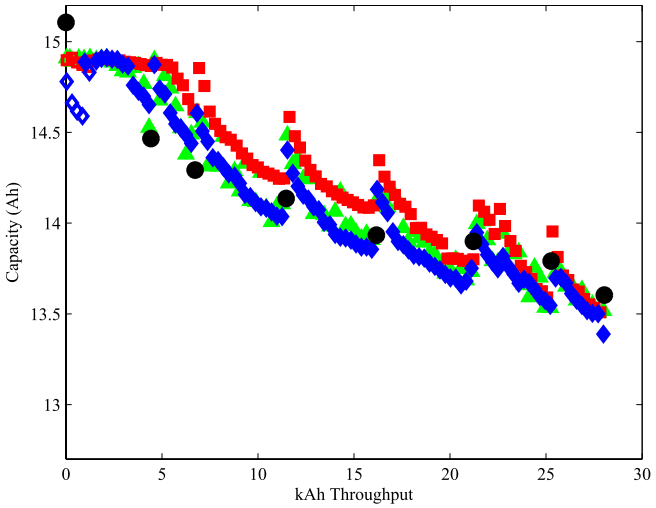

Fig. 13. Capacity estimation results for Cell 2 aged with a CD profile to 25% SOC charged at 3C/2.

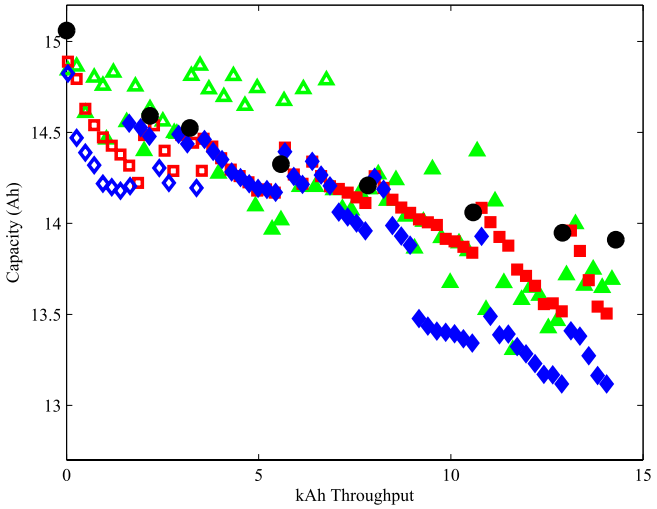

Fig. 15. Capacity estimation results for Cell 4 aged with a CD profile to 35% SOC charged at C/3.

around a day while the capacity assessments were carried out, allowing some capacity recovery.

Overall, the capacity estimates are more accurate and have a lower variance for cells that discharged to the low-SOC region (Cells 1–3). This result is expected, since the estimates should be less sensitive to model and sensor errors in the low-SOC region. In addition, the mid-SOC range is relatively small (only spans a normalized concentration of 0.07), so it becomes more difficult to decide when the estimate is truly converged. Essentially, there is a chance of missing this mid-SOC region, and taking the estimate too early in the discharge (when the estimate has not yet converged) or too late (when the estimate is starting to diverge again). At BOL, Cells 4 and 5 are not discharged sufficiently to reach the low-SOC region, so the initial estimates for these cells are taken in the mid-SOC region. However, as the estimated x_0 decreases over time, the end of the CD cycles begin to cross the threshold into the low-SOC region, at which point the algorithm switches to estimate in the low-SOC region. An important point here is that although the estimated concentration may cross into the low-SOC region, triggering the switch, the actual cell may not have done so. This is most likely the case for Cell 5, which is only discharged to 45% SOC. Right before the switch to an estimate at low-SOC is made, near the end of the test, the estimated capacities happen to be lower than the measured capacity (at least for the EKF and smoother). This means that the switch is made prematurely resulting in additional inaccuracies in the estimate after the switch is made. That said, the EKF and smoother eventually switch back to estimating in the mid-SOC region, tending to oscillate between the two regions. These problems illustrate the difficulty in relying on an imperfect estimate to determine if thresholds have been crossed.

In comparing the three observer types, there are no large differences in the estimate error mean or variance among the observers. The particle filter tends to produce slightly

TABLE III
CAPACITY ESTIMATION RESULTS

Cell	Test Condition	Observer	Estimate Error* Mean (Ah)	Estimate Error* Variance (Ah^2)	Normalized Computation Time
1	CD to 25% SOC, C/3 Charge	EKF	-0.08	0.020	1.00
		Kalman Smoother	0.18	0.023	1.14
		Particle Filter	-0.04	0.022	1.81
2	CD to 25% SOC, 3C/2 Charge	EKF	-0.01	0.026	1.00
		Kalman Smoother	0.15	0.031	1.15
		Particle Filter	0.05	0.027	1.82
3	CD to 25% SOC, 5C Charge	EKF	-0.47	0.012	1.00
		Kalman Smoother	-0.32	0.019	1.13
		Particle Filter	-0.17	0.028	1.78
4	CD to 35% SOC, C/3 Charge	EKF	-0.37	0.081	1.00
		Kalman Smoother	-0.16	0.019	1.13
		Particle Filter	-0.07	0.076	1.79
5	CD to 45% SOC, C/3 Charge	EKF	-0.48	0.073	1.00
		Kalman Smoother	-0.38	0.024	1.13
		Particle Filter	-0.00	0.081	1.78

*Estimate error defined as the difference between each estimate and a capacity interpolated between the periodic measured capacity assessments.

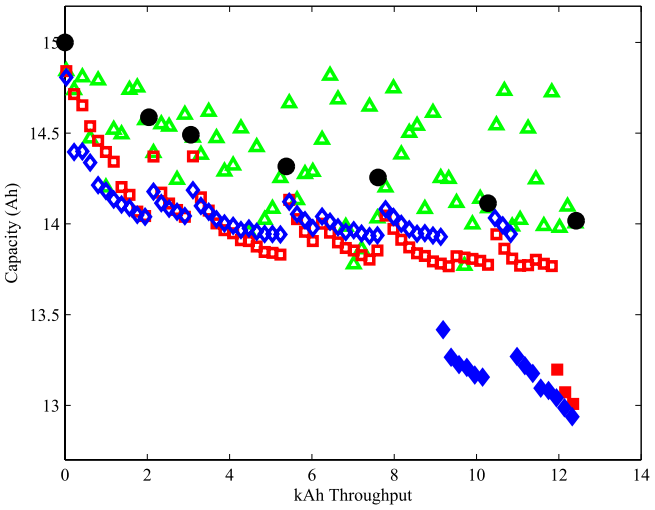

Fig. 16. Capacity estimation results for Cell 5 aged with a CD profile to 45% SOC charged at C/3.

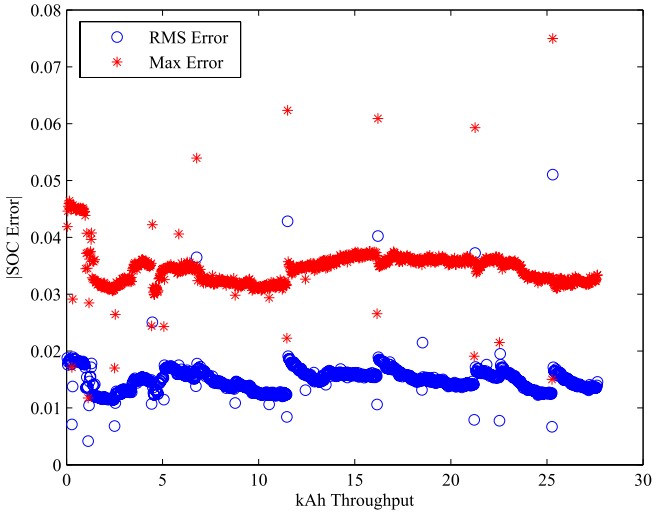

Fig. 17. Root mean square and maximum SOC estimate error for Cell 2. Each point indicates the error over a single CD-CCCV profile.

more accurate but noisier estimates than the other observers, particularly when estimating in the mid-SOC region. Overall, the EKF performs well without the additional computational effort required for the smoother and particle filter.

1) Maintaining SOC Accuracy: In addition to estimating cell capacity, another important objective in estimating the changes in model parameters corresponding to the dominant degradation mode within a cell (e.g., x_0 as it relates to loss of cyclable Li) is to maintain an accurate model over time, thereby maintaining an accurate SOC estimate over time. Fig. 17 shows how the accuracy of the SOC estimate changes over time for Cell 2 (the other cells showed a similar result). The estimated x_0 is used to update the model after each CD cycle, and as described previously, the SOC estimation is done using the EKF on the positive electrode submodel. The capacity used to calculate the measured SOC by Coulomb counting is obtained by interpolating between each periodic capacity assessment.

The SOC estimate error over a given CD-CCCV profile remains fairly constant throughout the life of the cell, indicating that the model is being updated correctly with estimates of x_0. Note that the outliers in the plot are instances where the profile had two CCCV charge portions, over which the model is less accurate.

IX. CONCLUSION

In this paper, a reduced-order electrochemical model for a composite electrode battery was applied in a dual-observer algorithm to estimate SOC and capacity. The estimates were validated against experimentally measured cell SOC and capacity over the course of an aging campaign. The capacity estimation algorithm performs well as long as the cell is discharged to a sufficiently low SOC, where the negative electrode OCV is steep and state estimates are less sensitive to voltage errors. Estimates taken in the mid-SOC range produced less reliable capacity estimates despite the small window of relatively steep OCV in this range. There was not

TABLE IV
EXPRESSIONS FOR LIE DERIVATIVES AND OBSERVABILITY MATRIX

$$l(x) = \begin{bmatrix} g \\ \dot{g} \\ \ddot{g} \end{bmatrix} = \begin{bmatrix} \frac{s_3 c(x)^3}{c_{max}^3} + \frac{s_2 c(x)}{c_{max}^2} + \frac{s_1 c(x)}{c_{max}} + s_0 \\ \frac{3 s_0 c(x)^2 \left(a_0 x_2 + a_1 x_3 + a_2 \left(\frac{x_2}{b_3} + \frac{b_2 x_3}{b_3}\right)\right)}{c_{max}^3} + \frac{2 s_1 c(x) \left(a_0 x_2 + a_1 x_3 + a_2 \left(\frac{x_2}{b_3} + \frac{b_2 x_3}{b_3}\right)\right)}{c_{max}^2} + \frac{s_2 \left(a_0 x_2 + a_1 x_3 + a_2 \left(\frac{x_2}{b_3} + \frac{b_2 x_3}{b_3}\right)\right)}{c_{max}} \\ \ddot{g} \end{bmatrix}$$

$$\mathcal{O} = \begin{bmatrix} \frac{3 s_0 c(x)^2 a_0}{c_{max}^3} + \frac{2 s_1 c(x) a_0}{c_{max}^2} + \frac{s_2 a_0}{c_{max}} & \frac{3 s_0 c(x)^2 a_1}{c_{max}^3} + \frac{2 s_1 c(x) a_1}{c_{max}^2} + \frac{s_2 a_1}{c_{max}} & \frac{3 s_0 c(x)^2 a_2}{c_{max}^3} + \frac{2 s_1 c(x) a_2}{c_{max}^2} + \frac{s_2 a_2}{c_{max}} \\ \frac{\partial \dot{g}}{\partial x_1} & \frac{\partial \dot{g}}{\partial x_2} & \frac{\partial \dot{g}}{\partial x_3} \\ \frac{\partial \ddot{g}}{\partial x_1} & \frac{\partial \ddot{g}}{\partial x_2} & \frac{\partial \ddot{g}}{\partial x_3} \end{bmatrix}$$

a significant improvement in the capacity estimation accuracy when using the more computationally expensive Kalman smoother and particle filter over the simpler EKF. Further estimation accuracy could be achieved with greater knowledge of the model parameters, but this paper demonstrates that the EKF approach is an attractive option for onboard SOH estimation. Future work in this area will focus on capacity and available power estimation in the presence of multiple degradation modes, i.e., if both cyclable lithium and active material are lost simultaneously.

APPENDIX
MODEL OBSERVABILITY CALCULATIONS

The nonlinear output equation for the single particle system makes calculation of the Lie derivatives and observability matrix tedious. An attempt will be made here to at least outline the process of calculating each element in the observability matrix, even though the entire matrix cannot be shown. Zero current will be assumed to reduce the length of the expressions, thereby eliminating the charge transfer and ohmic overpotential terms. This results in the following simplification of the dynamics and output equation (dropping the subscript i):

$$\begin{bmatrix} \dot{x}_1 \\ \dot{x}_2 \\ \dot{x}_3 \end{bmatrix} = f(x) = \begin{bmatrix} 0 & 1 & 0 \\ 0 & 0 & 1 \\ 0 & \frac{1}{b_3} & \frac{b_2}{b_3} \end{bmatrix} \begin{bmatrix} x_1 \\ x_2 \\ x_3 \end{bmatrix} \tag{30}$$

$$g(x) = \frac{s_3 c(x)^3}{c_{\max}^3} + \frac{s_2 c(x)}{c_{\max}^2} + \frac{s_1 c(x)}{c_{\max}} + s_0 \tag{31}$$

where the substitution $c(x) = a_0 x_1 + a_1 x_2 + a_2 x_3$ has been made. The first Lie derivative and the first row of the observability matrix are shown in Table IV, without expanding the other matrix elements. Again, it should be made clear that the calculation of the complete observability matrix, without assuming zero current, was done using symbolic manipulation software resulting in a matrix with full rank.

REFERENCES

[1] N. A. Chaturvedi, R. Klein, J. Christensen, J. Ahmed, and A. Kojic, "Algorithms for advanced battery-management systems," *IEEE Control Syst. Mag.*, vol. 30, no. 3, pp. 49–68, Jun. 2010.

[2] R. Klein, N. A. Chaturvedi, J. Christensen, J. Ahmed, R. Findeisen, and A. Kojic, "Electrochemical model based observer design for a lithium-ion battery," *IEEE Trans. Control Syst. Technol.*, vol. 21, no. 2, pp. 289–301, Mar. 2013.

[3] Y. Hu, S. Yurkovich, Y. Guezennec, and B. J. Yurkovich, "Electro-thermal battery model identification for automotive applications," *J. Power Sour.*, vol. 196, no. 1, pp. 449–457, 2011.

[4] S. Onori, P. Spagnol, V. Marano, Y. Guezennec, and G. Rizzoni, "A new life estimation method for lithium-ion batteries in plug-in hybrid electric vehicles applications," *Int. J. Power Electron.*, vol. 4, no. 3, pp. 302–319, 2012.

[5] G. L. Plett, "Extended Kalman filtering for battery management systems of LiPB-based HEV battery packs: Part 1. Background," *J. Power Sour.*, vol. 134, no. 12, pp. 252–261, 2004.

[6] G. L. Plett, "Extended Kalman filtering for battery management systems of LiPB-based HEV battery packs: Part 2. Modeling and identification," *J. Power Sour.*, vol. 134, no. 2, pp. 262–276, 2004.

[7] G. L. Plett, "Extended Kalman filtering for battery management systems of LiPB-based HEV battery packs: Part 3. State and parameter estimation," *J. Power Sour.*, vol. 134, no. 2, pp. 277–292, 2004.

[8] M. Rubagotti, S. Onori, and G. Rizzoni, "Automotive battery prognostics using dual extended Kalman filter," in *Proc. ASME DSCC*, Hollywood, CA, USA, Oct. 2009, pp. 257–263.

[9] M. F. Samadi, S. M. M. Alavi, and M. Saif, "An electrochemical model-based particle filter approach for lithium-ion battery estimation," in *Proc. IEEE 51st Annu. Conf. Decision Control*, Maui, HI, USA, Dec. 2012, pp. 3074–3079.

[10] Y. Hu and S. Yurkovich, "Battery cell state-of-charge estimation using linear parameter varying system techniques," *J. Power Sour.*, vol. 198, pp. 338–350, Jan. 2012.

[11] M. Doyle, T. F. Fuller, and J. Newman, "Modeling of galvanostatic charge and discharge of the lithium/polymer/insertion cell," *J. Electrochem. Soc.*, vol. 140, no. 6, pp. 1526–1533, 1993.

[12] J. Marcicki, A. Bartlett, A. T. Conlisk, G. Rizzoni, X. G. Yang, and T. Miller, "Robustness evaluation for state-of-charge and state-of-health estimation considering electrochemical parameter uncertainties," in *Proc. Amer. Control Conf.*, Washington, DC, USA, Jun. 2013, pp. 686–691.

[13] K. A. Smith, C. D. Rahn, and C.-Y. Wang, "Model-based electrochemical estimation and constraint management for pulse operation of lithium ion batteries," *IEEE Trans. Control Syst. Technol.*, vol. 18, no. 3, pp. 654–663, May 2010.

[14] D. Di Domenico, A. Stefanopoulou, and G. Fiengo, "Lithium-ion battery state of charge and critical surface charge estimation using an electrochemical model-based extended Kalman filter," *J. Dyn. Syst., Meas., Control*, vol. 132, no. 6, p. 061302, 2010.

[15] S. Santhanagopalan, Q. Zhang, K. Kumaresan, and R. E. White, "Parameter estimation and life modeling of lithium-ion cells," *J. Electrochem. Soc.*, vol. 155, no. 4, pp. A345–A353, 2008.

[16] S. Santhanagopalan and R. E. White, "State of charge estimation using an unscented filter for high power lithium ion cells," *Int. J. Energy Res.*, vol. 34, no. 2, pp. 152–163, 2009.

[17] S. J. Moura, N. A. Chaturvedi, and M. Krstic, "Adaptive PDE observer for battery SOC/SOH estimation," in *Proc. ASME DSCC*, Fort Lauderdale, FL, USA, Oct. 2012.

[18] S. K. Rahimian, S. Rayman, and R. E. White, "State of charge and loss of active material estimation of a lithium ion cell under low earth orbit condition using Kalman filtering approaches," *J. Electrochem. Soc.*, vol. 159, no. 6, pp. A860–A872, 2012.

[19] A. P. Schmidt, M. Bitzer, A. W. Imre, and L. Guzzella, "Model-based distinction and quantification of capacity loss and rate capability fade in Li-ion batteries," *J. Power Sour.*, vol. 195, no. 22, pp. 7634–7638, 2010.
[20] A. Bartlett, J. Marcicki, S. Onori, G. Rizzoni, X. G. Yang, and T. Miller, "Model-based state of charge estimation and observability analysis of a composite electrode lithium-ion battery," in *Proc. IEEE 52nd Annu. Conf. Decision Control*, Florence, Italy, Dec. 2013, pp. 7791–7796.
[21] J. Marcicki, M. Canova, A. T. Conlisk, and G. Rizzoni, "Design and parametrization analysis of a reduced-order electrochemical model of graphite/$LiFePO_4$ cells for SOC/SOH estimation," *J. Power Sour.*, vol. 237, pp. 310–324, Sep. 2013.
[22] J. Marcicki, F. Todeschini, S. Onori, and M. Canova, "Nonlinear parameter estimation for capacity fade in lithium-ion cells based on a reduced-order electrochemical model," in *Proc. Amer. Control Conf. (ACC)*, Montreal, QC, Canada, Jun. 2012, pp. 572–577.
[23] J. Marcicki *et al.*, "Characterization of cycle-life aging in automotive lithium-ion pouch cells," *Electrochem. Soc. Trans.*, vol. 50, no. 26, pp. 235–247, 2013.
[24] J. C. Forman, S. Bashash, J. L. Stein, and H. K. Fathy, "Reduction of an electrochemistry-based li-ion battery model via quasi-linearization and Padé approximation," *J. Electrochem. Soc.*, vol. 158, no. 2, pp. A93–A101, 2011.
[25] K.-W. Nam, W.-S. Yoon, H. Shin, K. Y. Chung, S. Choi, and X.-Q. Yang, "*In situ* X-ray diffraction studies of mixed $LiMn_2O_4$–$LiNi_{1/3}Co_{1/3}Mn_{1/3}O_2$ composite cathode in Li-ion cells during charge–discharge cycling," *J. Power Sour.*, vol. 192, no. 2, pp. 652–659, 2009.
[26] A. Isidori, *Nonlinear Control Systems: An Introduction*, 3rd ed. London, U.K.: Springer-Verlag, 1995.
[27] *United States Department of Energy Battery Test Manual for Plug-In Hybrid Electric Vehicles, Revision 1*, document INL EXT-07-12535, 2010.
[28] D. Kim *et al.*, "Re-deposition of manganese species on spinel $LiMn_2O_4$ electrode after Mn dissolution," *J. Electrochem. Soc.*, vol. 159, no. 3, pp. A193–A197, 2012.
[29] K. M. Shaju, G. V. Subba Rao, and B. V. R. Chowdari, "Influence of Li-ion kinetics in the cathodic performance of layered $Li(Ni_{1/3}Co_{1/3}Mn_{1/3})O_2$," *J. Electrochem. Soc.*, vol. 151, no. 9, pp. A1324–A1332, 2004.
[30] D. Simon, *Optimal State Estimation: Kalman, H Infinity, and Nonlinear Approaches*. Hoboken, NJ, USA: Wiley, 2006.
[31] M. S. Arulampalam, S. Maskell, N. Gordon, and T. Clapp, "A tutorial on particle filters for online nonlinear/non-Gaussian Bayesian tracking," *IEEE Trans. Signal Process.*, vol. 50, no. 2, pp. 174–188, Feb. 2002.
[32] N. J. Gordon, D. J. Salmond, and A. F. M. Smith, "Novel approach to nonlinear/non-Gaussian Bayesian state estimation," *IEE Proc.-F Radar Signal Process.*, vol. 140, no. 2, pp. 107–113, Apr. 1993.
[33] M. Dubarry *et al.*, "Evaluation of commercial lithium-ion cells based on composite positive electrode for plug-in hybrid electric vehicle applications. Part I: Initial characterizations," *J. Power Sour.*, vol. 196, no. 23, pp. 10328–10335, 2011.
[34] M. Dubarry *et al.*, "Evaluation of commercial lithium-ion cells based on composite positive electrode for plug-in hybrid electric vehicle applications. Part II. Degradation mechanism under 2 C cycle aging," *J. Power Sour.*, vol. 196, no. 23, pp. 10336–10343, 2011.
[35] J. L. Crassidis and J. L. Junkins, *Optimal Estimation of Dynamic Systems*. Boca Raton, FL, USA: CRC Press, 2004.

Alexander Bartlett received the B.S. degree in mechanical engineering from the University of Michigan, Ann Arbor, MI, USA, in 2011. He is currently pursuing the Ph.D. degree with The Ohio State University, Columbus, OH, USA.

He is with Ford Motor Company, Dearborn, MI, USA, through the Ford University Research Program. His current research interests include modeling, control, and estimation of automotive batteries.

James Marcicki received the B.S. and M.S. degrees from the Department of Mechanical Engineering, University of Michigan, Ann Arbor, MI, USA, in 2008 and 2009, respectively, and the Ph.D. degree from The Ohio State University, Columbus, OH, USA, in 2012.

He is currently with the Research and Innovation Center, Ford Motor Company, Dearborn, MI, USA. His current research interests include modeling and characterization of energy storage systems, with a focus on secondary batteries.

Simona Onori received the Laurea (*summa cum laude*) degree in computer engineering from the University of Rome Tor Vergata, Rome, Italy, in 2003, the M.S. degree in electrical and computer engineering from the University of New Mexico, Albuquerque, NM, USA, in 2004, and the Ph.D. degree in control engineering from the University of Rome Tor Vergata, in 2007.

She was with IBM, Rome, from 2000 to 2002, and Thales-Alenia Space, Rome, in 2007. From 2007 to 2013, she was with the Center for Automotive Research, Ann Arbor, MI, USA. From 2010 to 2013, she was a Lecturer with the Department of Mechanical and Aerospace Engineering, The Ohio State University, Columbus, OH, USA. She is currently an Assistant Professor with the Department of Automotive Engineering, Clemson University, Greenville, SC, USA. Her background is in control system theory. Her current research interests include ground vehicle propulsion systems, including electric and hybrid electric powertrains, electrochemical energy storage systems, and after treatment systems with an emphasis on modeling, simulation, optimization, and feedback control design.

Giorgio Rizzoni received the B.S., M.S., and Ph.D. degrees in electrical and computer engineering from the University of Michigan, Ann Arbor, MI, USA, in 1980, 1982, and 1986, respectively.

He was a Post-Doctoral Fellow, and then a Lecturer and an Assistant Research Scientist with the University of Michigan from 1986 to 1990. In 1990, he joined the Department of Mechanical and Aerospace Engineering, The Ohio State University, Columbus, OH, USA, as an Assistant Professor. He was promoted to Associate Professor and Professor in 1995 and 2000. In 1999, he was appointed as the Director of the Center for Automotive Research. Since 2002, he has held the Ford Motor Company Chair in Electromechanical Systems, and has also been appointed as a Professor with the Department of Electrical and Computer Engineering. His specialization is in dynamic systems and control. His current research interests include sustainable and safe mobility.

Xiao Guang Yang received the B.S., M.S., and Ph.D. degrees in materials sciences and engineering from Zhejiang University, Hangzhou, China, in 1988, 1990, and 1995, respectively.

He was a Research Associate with the University of Hawaii, Honolulu, HI, USA, from 1999 to 2000, and Pennsylvania State University, State College, PA, USA, from 2002 to 2005. In 2005, he joined Ford Motor Company, Dearborn, MI, USA, as a Product Engineer for Hybrid Electric Vehicle programs. In 2010, he became a Technical Expert in Advanced Battery Technologies with the Department of Energy Storage and Materials Research, Research and Advanced Engineering, Ford Motor Company. He is currently involved in battery development, benchmark testing, model simulation, and validation.

Dr. Yang has been a Technical Advisory Member of the United States Advanced Battery Consortium Technical Committee since 2008.

Ted Miller is currently a Senior Manager of Energy Storage and Materials Strategy and Research with Ford Motor Company, Dearborn, MI, USA. His team is responsible for energy storage strategy, research, development, and implementation for all Ford hybrid, plug-in hybrid, battery electric, and fuel cell vehicles. His team supports global prototype and production vehicle development programs, and they are involved in every aspect of energy storage design and use from raw materials to end-of-life recycling. His team also sponsors collaborative research programs with the University of Michigan, Ann Arbor, MI, USA, where they will soon be opening a new joint battery fabrication and evaluation laboratory, Stanford, MIT, The Ohio State University, and a number of other major universities worldwide. He holds a number of energy storage technology patents, and has authored many published papers in the field, and is an experienced speaker on advanced energy storage technology and materials.

Mr. Miller is the Chairman of the United States Advanced Battery Consortium Management Committee.